

Gravitational lensing properties of isothermal universal halo profile

Xinzhong Er¹

¹National Astronomical Observatories, Chinese Academy of Sciences, Beijing 100012, China;
xer@nao.ac.cn

Abstract N-body simulations predict that dark matter halos with different mass scales are described by a universal model, the Navarro-Frenk-White (NFW) density profiles. As a consequence of baryonic cooling effects, the halos will become more concentrated, and similar to an isothermal sphere over large range in radii ($\sim 300 h^{-1}\text{kpc}$). The singular isothermal sphere model however has to be truncated artificially at large radii since it extends to infinity. We model a massive galaxy halo as a combination of an isothermal sphere and an NFW density profile. We give an approximation for the mass concentration at different baryon fractions and present exact expressions for the weak lensing shear and flexion for such a halo. We compare the lensing properties with a Singular Isothermal Sphere and NFW profiles. We find that the combined profile can generate higher order lensing signals at small radii and is more efficient in generating strong lensing events. In order to distinguish such a halo profile from the SIS or NFW profiles, one needs to combine strong and weak lensing constraints on small and large radii.

Key words: Gravitational lensing; galaxies: halos; cosmology: dark matter

1 INTRODUCTION

The Cold Dark Matter with the cosmological constant model (Λ CDM) provides a successful description of many properties of observations of the universe. N-body simulations of Λ CDM models predict dark matter halos with a universal density profile (e.g. Navarro et al., 1997). The Navarro-Frenk-White (NFW) profile appears to be a good approximation for dark halo profiles over a wide range of masses. On the other hand, the NFW halo density profile can also be generalized with an arbitrary power law central cusp, and outer regions that fall off as r^{-3} (Jing & Suto, 2000). It also has been found that the slope of the inner regions steepens for smaller mass haloes. More importantly, baryonic cooling will significantly steepen the density profiles, close to the isothermal slopes observed (Koopmans et al., 2009). The baryon effect is more significant in the galaxy halo since it contains more baryons. A composite model with an NFW dark matter halo and a de Vaucouleurs stellar component is suggested for massive galaxies by Gavazzi et al. (2007). The total density profile is close to isothermal form over large range in radius ($\sim 300 h^{-1}\text{kpc}$). Therefore, we model the halo total mass profile as an Isothermal-NFW (INFW) profile, which is the combination of an NFW dark halo plus a stellar component at inner radii, i.e. $\rho \propto r^{-2}$ for small radius.

Gravitational lensing provides a direct way to study the mass distribution of large scale structures in the universe as well as galaxy and cluster halos. It probes the mass distribution independent of the nature of matter or its dynamical state (e.g. Bartelmann & Schneider, 2001; Treu, 2010). Lensing is widely used for the cluster mass reconstruction (e.g. Bradač et al., 2006), and galaxy halo measurement (e.g. Cacciato et al., 2009). Weak lensing is the physical phenomenon causing the weak image distortion of background galaxies. By comparing the image distortions with non-lensed image shapes, one can infer

the mass distribution of the foreground lens. In weak lensing, most studies consider the shear effect, which transfers a round source into an elliptical one. Higher order effects, flexion are gradually coming within reach. Flexion can be introduced as derivatives of either the surface mass density or the shear. They respond to smaller-scale variations in the projected mass distribution than the shear (Bacon et al., 2006). The convergence gradient, called the first flexion \mathcal{F} , introduces a centroid shift in the lensed image and is a spin-1 symmetry quantity, while the second flexion \mathcal{G} is the gradient of shear and is spin-3. Flexion provides a measure of small scale variations of mass distribution as well as the halo ellipticity (Er & Schneider, 2011; Er et al., 2012).

The lensing properties of different halo profiles have been widely studied, e.g. the NFW profile (Bartelmann, 1996) and the Einasto profile (Retana-Montenegro et al., 2012). Wyithe et al. (2001) and Keeton & Madau (2001) have studied a generalized NFW type profile for lensing. Therefore, it is interesting to use the INFW profile as a galaxy halo, and it is natural to extend its applications to the gravitational lensing characteristics of dark matter halos. For first time, we apply analytical and numerical methods to the gravitational lensing study of INFW halo profiles. In Sect.2, we present the basic halo properties of the INFW profile. In Sect.3, the analytical formula of an INFW lens halo is given. We compare the INFW profile with other models in Sect.4 and give a summary at the end. The cosmology that we adopt in this paper is a Λ CDM model with parameters based on the results of the Wilkinson Microwave Anisotropy Probe seven year data (Komatsu et al., 2011): $\Omega_\Lambda = 0.734$, $\Omega_m = 0.266$, Hubble constant $H_0 = 100h \text{ km s}^{-1} \text{ Mpc}^{-1}$ and $h = 0.71$.

2 INFW HALO PROPERTIES

In analogy to NFW model, the density profile of INFW is given by

$$\rho(r) = \frac{\rho_c \Delta'_c r_s^3}{r^2 (r_s + r)}, \quad (1)$$

where $\rho_c = 3H(z)^2/(8\pi G)$ is the critical density of the universe, $H(z)$ is the Hubble parameter, and G is Newton's constant. The dimensionless characteristic density is given by

$$\Delta'_c = \frac{200c_I^3}{3\ln(1+c_I)} \quad (2)$$

(see, e.g., Wyithe et al., 2001). We will use the same definition for the concentration $c_I = r_{200}/r_s$, where r_s is the scale radius. The virial radius r_{200} is defined as the radius inside which the mass density of the halo is equal to $200\rho_c$ (Navarro et al., 1997). The mass of a halo contained within a radius of r_{200} is thus

$$M_{200} = \frac{800\pi}{3} \rho_c r_{200}^3. \quad (3)$$

There is no specific study or simulations for the relationship between mass and concentration for generalized-NFW profiles. We assume that initially dark matter and baryons follow the same NFW profile. Due to the cooling effect, baryons collapse toward the center of the dark matter halo, and steepen the inner density profile. We assume the collapsed baryons make a fraction f_b of the total mass. The outer density of the INFW profile will become lower by a factor of $(1 - f_b)$: $\rho_{\text{INFW}}(r_{200}) = (1 - f_b)\rho_{\text{NFW}}(r_{200})$. We take f_b as the universal baryon fraction, although a lower number does not change the scaling significantly. A relation between c and c_I can be obtained from

$$\frac{c_I}{\ln(1+c_I)(1+c_I)} = (1-f_b) \frac{c^2}{\left[\ln(1+c) - \frac{c}{1+c}\right](1+c)^2}. \quad (4)$$

This relation can be solved numerically. It can be also approximated by

$$c_I = \frac{c}{3-6f_b} - \frac{3-6f_b}{c}. \quad (5)$$

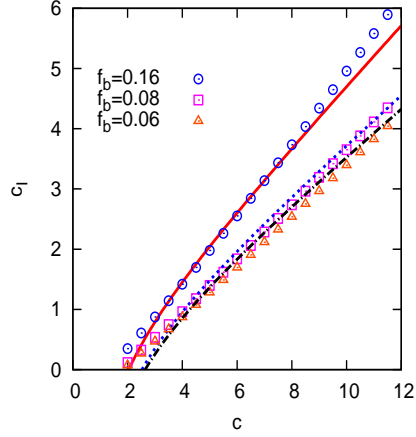


Fig. 1 The approximate relationship between the concentration c for the NFW profile and c_I for the INFW profile. The points are the numerical results from solving Eq.(4) for different baryon fractions: $f_b = 0.16$ (circles), $f_b = 0.08$ (squares) and $f_b = 0.06$ (triangles). The lines are the approximate relationship using Eq.(5).

In Fig. 1, one can see that our approximation mainly agrees with the numerical results. A smaller baryon fraction will lead to a lower concentration of the INFW halo. When the concentration c_I becomes to 0, $r_s \rightarrow \infty$, and the INFW profile reduces to an SIS. Thus in general the INFW profile is more concentrated than SIS profile at small radial. We will see in next section that the INFW profile can produce higher lensing signals and is more efficient in generating strong lensing than other profiles. The small variation of baryon fraction does not strongly affect the matter density profile (right panel of Fig. 2). With higher baryon fraction, the density at inner radius is larger. In the rest of the paper, we will use $f_b = 0.16$ and Eq.(5) to estimate the concentration of the INFW halo.

In left panel of Fig. 2 we show $\rho(r)$ for three different halo profiles using same halo mass M_{200} . One can see that the INFW profile has the same slope as SIS at small radii ($< 30 h^{-1}$ kpc) and approaches to NFW at large radii.

3 LENSING PROPERTIES OF INFW HALO

3.1 Basic lensing formula

The fundamentals of gravitational lensing can be found in Bartelmann & Schneider (2001). For its elegance and brevity, we shall use the complex notation. The thin-lens approximation is adopted, implying that the lensing mass distribution can be projected onto the lens plane perpendicular to the line-of-sight. We introduce angular coordinates θ on the lensing plane with respect to the line-of-sight. The lensing convergence, that is the dimensionless projected surface-mass density, can be written as

$$\kappa(\theta) = \Sigma(\theta)/\Sigma_{\text{cr}}, \quad \text{where} \quad \Sigma_{\text{cr}} = \frac{c^2}{4\pi G} \frac{D_s}{D_d D_{\text{ds}}} \quad (6)$$

is the critical surface mass density depending on the angular-diameter distances D_s , D_d and D_{ds} from the observer to the source, the observer to the lens, and the lens to the source, respectively. $\Sigma(\theta)$ is the projected surface-mass density of the lens. All lensing quantities can be derived from the effective lensing potential ψ ,

$$\psi(\theta) = \frac{1}{\pi} \int_{\mathcal{R}^2} d^2\theta' \kappa(\theta') \ln|\theta - \theta'|. \quad (7)$$

The lens equation is given by

$$\beta = \theta - \alpha(\theta), \quad (8)$$

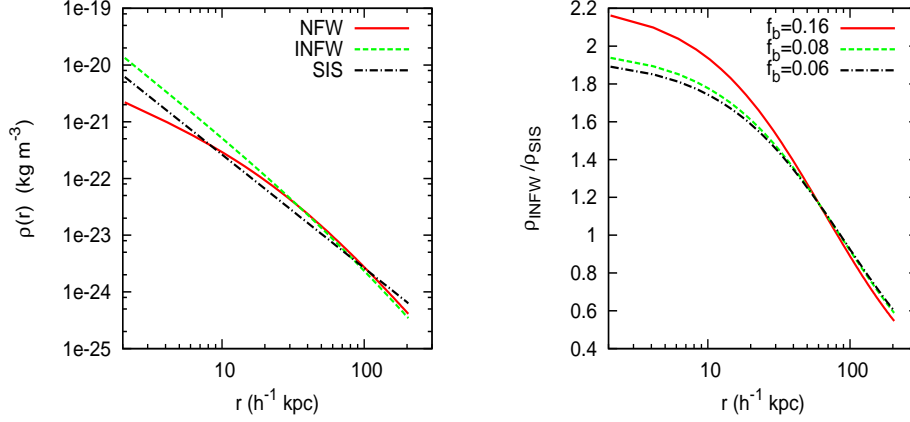


Fig. 2 Left panel: halo mass density $\rho(r)$ for three different profiles: NFW (solid line), INFW (dashed line), SIS (dot-dashed line). The same mass ($M_{200} = 10^{12} h^{-1} M_{\odot}$) is used for different profiles (also for right panel). The concentration is $c = 6.95$ ($c_I = 3.11$, $f_b = 0.16$) for NFW (INFW) halo. Right panel: $\rho(r)_{\text{INFW}}/\rho(r)_{\text{SIS}}$ with different f_b : 0.16 (solid line), 0.08 (dashed line), 0.06 (dot-dashed line).

where β is the source position and α is the deflection angle

$$\alpha = \nabla_c \psi, \quad (9)$$

where the complex differential operators is defined as

$$\nabla_c := \frac{\partial}{\partial \theta_1} + i \frac{\partial}{\partial \theta_2}; \quad \nabla_c^* := \frac{\partial}{\partial \theta_1} - i \frac{\partial}{\partial \theta_2}. \quad (10)$$

To the lowest order, image distortions caused by gravitational lensing are described by the complex shear and convergence (which equals to the dimensionless surface mass density)

$$\gamma = \frac{1}{2} (\partial_1^2 \psi - \partial_2^2 \psi) + i \partial_1 \partial_2 \psi = \frac{1}{2} \nabla_c^2 \psi; \quad \kappa = \frac{1}{2} (\partial_1^2 \psi + \partial_2^2 \psi) = \frac{1}{2} \nabla_c \nabla_c^* \psi, \quad (11)$$

where the subscripts i denote partial derivatives with respect to θ_i . The magnification for a point source is thus given by

$$\mu = \frac{1}{(1 - \kappa)^2 - |\gamma|^2}. \quad (12)$$

The shear transforms a hypothetical round source into an elliptical image. The \mathcal{F} and \mathcal{G} flexions can be introduced as the complex derivatives

$$\mathcal{F} = \nabla_c \kappa; \quad \mathcal{G} = \nabla_c \gamma. \quad (13)$$

The flexions are thus combinations of third-order derivatives of the effective lensing potential ψ . We shall denote their real and imaginary parts by $(\mathcal{F}, \mathcal{G})_1$ and $(\mathcal{F}, \mathcal{G})_2$, respectively. In terms of the lensing potential, we have

$$\mathcal{F} \equiv \mathcal{F}_1 + i \mathcal{F}_2 = \frac{1}{2} (\partial_1^3 \psi + \partial_1 \partial_2^2 \psi) + \frac{i}{2} (\partial_1^2 \partial_2 \psi + \partial_2^3 \psi) \quad (14)$$

and

$$\mathcal{G} \equiv \mathcal{G}_1 + i \mathcal{G}_2 = \frac{1}{2} (\partial_1^3 \psi - 3 \partial_1 \partial_2^2 \psi) + \frac{i}{2} (3 \partial_1^2 \partial_2 \psi - \partial_2^3 \psi). \quad (15)$$

3.2 Lensing of INFW halo

We derive the analytical expression for the lensing properties of INFW halo. The surface mass density of a spherically symmetric lens is obtained by integrating along the line of sight of the three-dimensional density profile,

$$\Sigma(\xi) = \int_{-\infty}^{\infty} \rho(\sqrt{\xi^2 + z^2}) dz, \quad (16)$$

where ξ is the distance from the center of the lens in the projected lens plane $\xi = \theta D_s$. It implies the following form for the dimensionless surface mass density

$$\kappa(x) = 2\kappa_s \left(\frac{\pi}{2x} - f(x) \right), \quad (17)$$

where $x = \theta/\theta_s$ ($\theta_s = r_s/D_d$), and $f(x)$ is given by

$$f(x) = \begin{cases} \frac{\operatorname{arcsech} x}{\sqrt{1-x^2}} & (x < 1); \\ 1 & (x = 1); \\ \frac{\operatorname{arcsec} x}{\sqrt{x^2-1}} & (x > 1). \end{cases} \quad (18)$$

In the spherical case, the deflection angle is given by

$$\alpha(\theta) = \frac{2}{\theta} \int_0^\theta \theta d\theta \kappa(\theta) = \frac{4\kappa_s \theta_s}{x} \left(\frac{\pi x}{2} + (1-x^2)f(x) + \ln \frac{x}{2} \right). \quad (19)$$

The analytical form of the shear can be calculated from $\gamma(\theta) = [\bar{\kappa}(\theta) - \kappa(\theta)] \exp[2i\phi]$, where ϕ is the polar angle. $\bar{\kappa}(\theta)$ is the mean surface mass density within a circle of radius of θ from the lens center (see e.g. Bartelmann & Schneider, 2001). The expression for shear due to the INFW is

$$\gamma(x) = 2\kappa_s \left[\frac{\pi}{2x} + \frac{2\ln(x/2)}{x^2} + \frac{2-x^2}{x^2} f(x) \right] e^{2i\phi}, \quad (20)$$

where $f(x)$ is defined in Eq. (18). The analytical form of two flexions can be also given

$$\mathcal{F}(x) = \frac{2\kappa_s}{\theta_s} \left[\frac{x f(x)}{x^2-1} - \frac{\pi}{2x^2} - \frac{1}{x(x^2-1)} \right] e^{i\phi}, \quad (21)$$

$$\mathcal{G}(x) = \frac{2\kappa_s}{\theta_s} \left(-\frac{3\pi}{2x^2} - \frac{8\ln(x/2)}{x^3} + \frac{1}{x(x^2-1)} - f(x) \left[\frac{8}{x^3} - \frac{3}{x} + \frac{1}{x(x^2-1)} \right] \right) e^{3i\phi}. \quad (22)$$

The elliptical INFW lensing properties can be calculated numerically (Keeton, 2001).

Furthermore, as pointed out by Schneider & Seitz (1995); Schneider & Er (2008), due to the mass-sheet degeneracy, the directly measurable properties are the reduced shear and reduced flexion

$$g = \frac{\gamma}{1-\kappa}; \quad G_1 = \frac{\mathcal{F} + g\mathcal{F}^*}{1-\kappa}; \quad G_3 = \frac{\mathcal{G} + g\mathcal{G}}{1-\kappa}. \quad (23)$$

The weak lensing properties of the INFW profile also show approximated behavior as a combination of two power-law profiles. At small radii, the asymptotic behavior can be approximated by a SIS, i.e. $\kappa, \gamma \propto \theta^{-1}$, and $\mathcal{F}, \mathcal{G} \propto \theta^{-2}$. At large radii, it behaves like the power-law $\rho \propto r^{-3}$. Thus the lensing signal rapidly fade out, $\kappa, \gamma \propto \theta^{-2}$, and $\mathcal{F}, \mathcal{G} \propto \theta^{-3}$.

4 PROFILES COMPARISONS

We compare the weak lensing properties for INFW, NFW, and SIS profiles. We use an approximation relation to calculate the mass concentration of the NFW profile (Neto et al., 2007)

$$c = 5.26 \left(\frac{M_{200}}{10^{14} h^{-1} M_{\odot}} \right)^{-0.1}, \quad (24)$$

and use Eq.5 to obtain c_I . The velocity dispersion of the SIS profile σ_v is calculated through $\sigma_v^3 = \frac{5}{\sqrt{2}} G H(z) M_{200}$ (Mo et al., 1998). The lensing properties of the SIS or NFW profiles can be found in e.g. Wright & Brainerd (2000); Schneider et al. (2006). We use lens halo mass $M_{200} = 10^{12} h^{-1} M_{\odot}$, which is a galactic sized halo. The lens is placed at redshift $z_d = 0.2$ and the sources are at redshift $z_s = 1.0$, which are accessible median redshifts for galaxy survey, e.g. SDSS or LSST. The concentration parameter for the NFW (INFW) profile in our test is $c = 6.95$ ($c_I = 3.11$). The Einstein radius of the SIS profile is $\theta_E \approx 0.3$ arcsec.

Fig. 3 shows the predicted convergence, reduced shear, first and second reduced flexions as a function of the angular separation from the lens center. The mass profile of the mock galaxy halo is assumed to be SIS (dotted line), NFW (dot-dashed line) and INFW (solid line) model. One can see that the overall behaviors of the three profiles are comparable. The asymptotic lensing behavior of the INFW profile are proportional to that of the SIS profile at small radii and approach NFW profile at large radii. The signal magnitudes of all lensing properties for the INFW halo are stronger than the other two at small radii but drop faster and eventually below that of the other two profiles. The differences between the magnitudes of the lensing signal are stronger at small radii than that at large radii. In particular, the shear and second flexion show a great dissimilarity. At large radii, the difference between three profiles is not significant.

In particular, the weak lensing properties of NFW halos is significantly different from the other two profiles at small radius (< 10 arcsec). The lensing signal of NFW is shallower than the others. On the other hand, the signal magnitude of INFW halo is about 2 times higher than that of SIS halo. The lensing signals of INFW drop faster with increasing radius, as one can see clearly from the first flexion (the convergence κ is not an observable quantity). Moreover, the angular separation at which the INFW halo first flexion is exceeded by other profiles is around 10 arcsec, and it is larger for shear and second flexion. In principle one can study the weak lensing signal, i.e. the shear and flexion to constrain the halo density profile. However, the weak lensing signal at large radii is small and hard to detect. On the other hand, it is also difficult to measure weak lensing signal when the background image is close to the lens galaxy. One can perform stacking method for galaxy-galaxy lensing studies. A large volume survey is necessary.

Moreover, the significant difference lensing properties at small radius will cause different strong lensing signal. In order to simply see the strong lensing properties, we compare the magnification cross sections for the three profiles. The cross section for a given magnification threshold is defined as

$$\sigma(\mu_{\min}) = \int_{|\mu| > \mu_{\min}} d^2\beta = \int_{|\mu| > \mu_{\min}} \frac{1}{|\mu|} d^2\theta. \quad (25)$$

In Fig. 4, the magnification cross section is shown in the left (right) panel for halo with mass $10^{13} h^{-1} M_{\odot}$ (different halo mass). We can see from both panels that the INFW profile can generate larger cross sections than the other two profiles, due to the high mass concentration of the INFW profile (top left panel in Fig. 3). The cross section of NFW halo increases faster with mass than other profiles, but decrease faster with μ . The curves of INFW and SIS profiles again have similar shapes, but the cross section of INFW halo is about two times larger than that of SIS halo for halo mass of $10^{13} h^{-1} M_{\odot}$. In additional tests, we also study the cross section of strong lensing multiple images. The probability generated by INFW halo can be several times higher than NFW halo, and will be easy to distinguish from each other. On the other hand, the INFW model generates about 3 times higher multiple image cross section than SIS model with halo mass $\sim 10^{12} h^{-1} M_{\odot}$ and approaches to that of SIS model for massive halo ($> 10^{15} h^{-1} M_{\odot}$). The concentration c_I becomes small for massive halo, thus

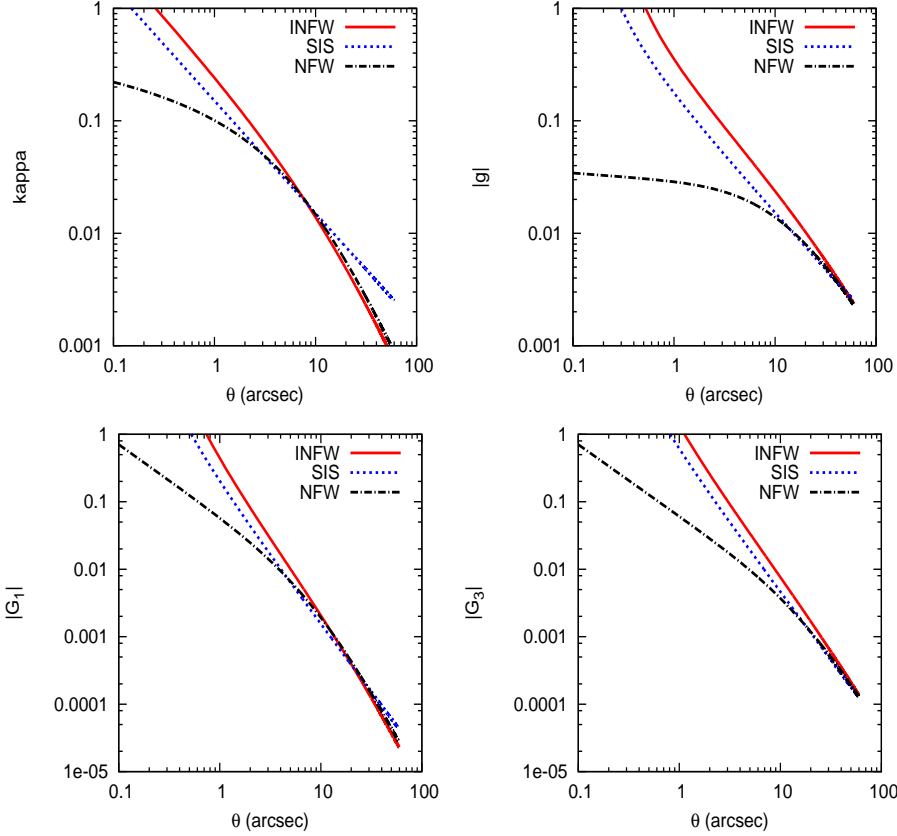


Fig. 3 Convergence, reduced shear and reduced flexions of three different profiles: INFW (solid line), SIS (dashed line), NFW (dot-dashed line). The mass of the lens halo is $M_{200} = 10^{12} h^{-1} M_{\odot}$. The lens and source redshifts are assumed to be $z_d = 0.2$ and $z_s = 1.0$ respectively.

the INFW nearly reduces to SIS profile. The multiple image separation generated by INFW lens can reach 4 arcsec for a halo mass of $10^{13} h^{-1} M_{\odot}$, which is about 40 percent larger than that generated by SIS lens. Therefore, the galaxy-galaxy strong lensing statistics can be a potential tool to distinguish INFW and SIS profile.

5 SUMMARY

We have studied the lensing properties of the INFW mass profile. The INFW profile is motivated by the combination of Cold Dark Matter simulations and a stellar component in the inner region of the dark matter halo, together with some evidence from observations (Gavazzi et al., 2007). The inner profile of INFW is isothermal, i.e. $\rho \propto r^{-2}$ and the outer profile is NFW-like $\rho \propto r^{-3}$. An approximate mass concentration due to different baryon fractions is given for the INFW profile, as a direct consequence of baryon collapse toward the center of halo.

The analytical expressions for deflection angle, convergence, shear and flexions of an INFW halo lens are given. We have compared the lensing properties of INFW profile with NFW and SIS halo profiles. We find that the INFW profile is more efficient than the others in generating lensing magnification, and the weak lensing signals of INFW halo is stronger at small radii than that of other profiles for the same halo mass. Strong lensing statistics can be used to constrain the lens profile, e.g. the image separa-

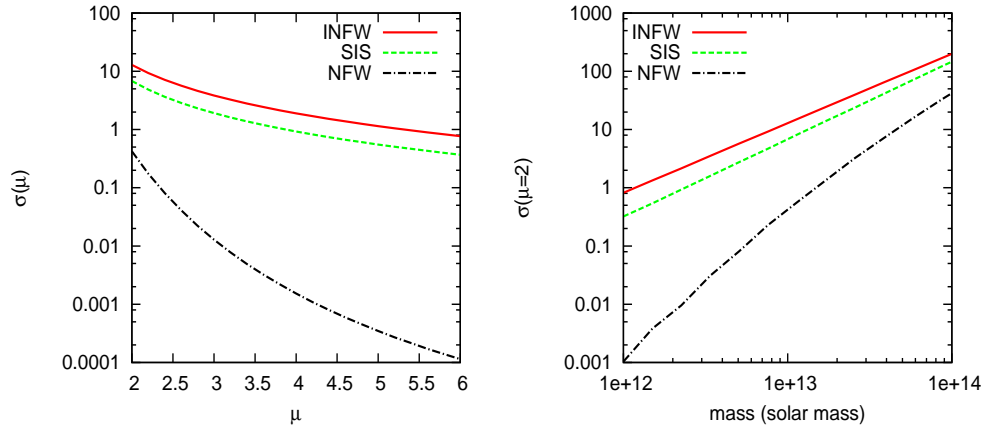


Fig. 4 The cross section of lensing magnification $\sigma(\mu)$ (in unit of arcsec^2) for three halo profiles: INFW (solid line), SIS (dashed line), NFW (dot-dashed line). The left panel shows the cross section as a function of lensing magnification for a lens halo with mass $M_{200} = 10^{13} h^{-1} M_{\odot}$. The right panel shows the cross section of given magnification ($\mu = 2$) for different lens halo mass. Same redshift condition of Fig.3 ($z_d = 0.2$, $z_s = 1.0$) is used.

tion. However, the image separation statistics is only sensitive to the inner profile of the lens halo. There is a degeneracy between the massive SIS lens and high concentrated INFW lens. Therefore, using weak lensing to study the large radial profile is essentially necessary.

Acknowledgements I thank Shude Mao, Ismael Tereno and Richard Long for discussions and comments on the manuscript. I also thank referee for comments and corrections on the manuscript.

References

- Bacon, D. J., Goldberg, D. M., Rowe, B. T. P., & Taylor, A. N. 2006, MNRAS, 365, 414
 Bartelmann, M. 1996, A&A, 313, 697
 Bartelmann, M., & Schneider, P. 2001, Phys. Rep., 340, 291
 Bradač, M., Clowe, D., Gonzalez, A. H., et al. 2006, ApJ, 652, 937
 Cacciato, M., van den Bosch, F. C., More, S., et al. 2009, MNRAS, 394, 929
 Er, X., & Schneider, P. 2011, A&A, 528, A52
 Er, X., Tereno, I., & Mao, S. 2012, MNRAS, 421, 1443
 Gavazzi, R., Treu, T., Rhodes, J. D., et al. 2007, ApJ, 667, 176
 Jing, Y. P., & Suto, Y. 2000, ApJ, 529, L69
 Keeton, C. R. 2001, ArXiv:astro-ph/0102341
 Keeton, C. R., & Madau, P. 2001, ApJ, 549, L25
 Komatsu, E., Smith, K. M., Dunkley, J., et al. 2011, ApJS, 192, 18
 Koopmans, L. V. E., Bolton, A., Treu, T., et al. 2009, ApJ, 703, L51
 Mo, H. J., Mao, S., & White, S. D. M. 1998, MNRAS, 295, 319
 Navarro, J. F., Frenk, C. S., & White, S. D. M. 1997, ApJ, 490, 493
 Neto, A. F., Gao, L., Bett, P., et al. 2007, MNRAS, 381, 1450
 Retana-Montenegro, E., Frutos-Alfaro, F., & Baes, M. 2012, A&A, 546, A32
 Schneider, P., & Er, X. 2008, A&A, 485, 363
 Schneider, P., Kochanek, C. S., & Wambsganss, J. 2006, Gravitational Lensing: Strong, Weak and Micro
 Schneider, P., & Seitz, C. 1995, A&A, 294, 411
 Treu, T. 2010, ARA&A, 48, 87
 Wright, C. O., & Brainerd, T. G. 2000, ApJ, 534, 34

Wyithe, J. S. B., Turner, E. L., & Spergel, D. N. 2001, *ApJ*, 555, 504